ResearchGate

See discussions, stats, and author profiles for this publication at:
https://www.researchgate.net/publication/263093147

Vibronic and Rydberg series assignments in the vacuum ultraviolet absorption spectrum of nitrous oxide

ARTICLE *in* JOURNAL OF QUANTITATIVE SPECTROSCOPY AND RADIATIVE TRANSFER · NOVEMBER 2014

Impact Factor: 2.65 · DOI: 10.1016/j.jqsrt.2014.05.017

CITATIONS
2

READS
71

7 AUTHORS, INCLUDING:

Aparna Shastri
Bhabha Atomic Research Centre
32 PUBLICATIONS **74** CITATIONS
SEE PROFILE

Param Jeet Singh
Bhabha Atomic Research Centre
26 PUBLICATIONS **53** CITATIONS
SEE PROFILE

Sunanda Krishnakumar
Bhabha Atomic Research Centre
1 PUBLICATION **2** CITATIONS
SEE PROFILE

Sekhar B.N.Raja
Raja Ramanna Centre for Advanced Te…
65 PUBLICATIONS **166** CITATIONS
SEE PROFILE

All in-text references underlined in blue are linked to publications on ResearchGate, letting you access and read them immediately.

Available from: Aparna Shastri
Retrieved on: 25 January 2016

Journal of Quantitative Spectroscopy & Radiative Transfer 147 (2014) 121–133

Contents lists available at ScienceDirect

Journal of Quantitative Spectroscopy & Radiative Transfer

journal homepage: www.elsevier.com/locate/jqsrt

Vibronic and Rydberg series assignments in the vacuum ultraviolet absorption spectrum of nitrous oxide

Aparna Shastri [a,*], Param Jeet Singh [a], Sunanda Krishnakumar [a], Anuvab Mandal [b], B.N. Raja Sekhar [a], R. D'Souza [a], B.N. Jagatap [b]

[a] Atomic and Molecular Physics Division, Bhabha Atomic Research Centre, Trombay, Mumbai 400085, India
[b] Homi Bhabha National Institute, Bhabha Atomic Research Centre, Trombay, Mumbai 400085, India

ARTICLE INFO

Article history:
Received 24 December 2013
Received in revised form
13 May 2014
Accepted 15 May 2014
Available online 24 May 2014

Keywords:
Vacuum ultraviolet
Synchrotron radiation
Nitrous oxide
Renner–Teller
Photoabsorption
Rydberg series

ABSTRACT

We report a comprehensive photoabsorption study of nitrous oxide (N_2O) in the vacuum ultraviolet (45,000–95,000 cm^{-1}) region using synchrotron radiation. The observed spectrum comprises of a few valence transitions and low lying Rydberg series converging to the two spin–orbit components ($^2\Pi_{1/2,3/2}$) of the ground state of N_2O^+. Spectral analysis is aided by extensive quantum chemical calculations of vertical excited states, oscillator strengths and potential energy curves using the time dependent density functional theory. Vibronic bands observed in the first absorption system (45,000–60,000 cm^{-1}) are assigned to hot band progressions in ν_2' originating from $\nu''=1$ or 2. New insights into the assignment of the well-formed progression of bands in the $X^1\Sigma^+ \rightarrow C^1\Pi$ system (60,000–72,000 cm^{-1}) are afforded by consideration of the Renner–Teller interaction. A set of molecular vibrational parameters ($\omega_2=467$ cm^{-1}, $x_{22}=-2.9$, $\varepsilon=-0.24$) for the $C^1\Pi$ state are derived from a fitting of the experimental data. The $3p\pi\,^1\Sigma^+$ state at ~77,600 cm^{-1} shows a large quantum defect (0.96) which is explained as arising due to mixed valence–Rydberg character. In the 85,000–95,000 cm^{-1} region, a number of absorption features are observed with greater clarity than in earlier photoabsorption studies and assigned to Rydberg series of type $nl\lambda$ ($n=3,4$; $l=s,p,d$; $\lambda=\sigma,\pi,\delta$) and accompanying vibronic bands. This work has resulted in clarification of several discrepancies in earlier Rydberg series assignments. Additionally, the $3p\pi\,^3\Sigma^-$ Rydberg state at 85,788 cm^{-1}, the valence transition $7\sigma\rightarrow3\pi$ ($^1\Pi$) at 87,433 cm^{-1} and the $3d\lambda$ Rydberg series in the 91,700–92,600 cm^{-1} region are assigned for the first time.

© 2014 Elsevier Ltd. All rights reserved.

1. Introduction

There has been continued interest in the nitrous oxide (N_2O) molecule due to its important role in atmospheric and astrophysical processes [1–5]. For example, the isotopic fractionation of nitrogen atoms in the upper atmosphere has been ascribed to the UV photodissociation dynamics of N_2O [3 and references therein]. Photodissociation of N_2O is known to produce metastable species such as O (^1S,^1D) which participate in important atmospheric photochemical reactions. Recent studies show that nitrous oxide is the single largest anthropogenic threat to the ozone layer in the 21st century and also has a very high global warming potential [1]. It has been found to be involved in the catalytic destruction of ozone in the stratosphere and to be the main source of odd nitrogen which regulates the ozone layer, and also could be the only

* Corresponding author. Tel.: +91 22 25590343; fax: +91 22 25502652.
E-mail address: ashastri@barc.gov.in (A. Shastri).

http://dx.doi.org/10.1016/j.jqsrt.2014.05.017
0022-4073/© 2014 Elsevier Ltd. All rights reserved.

interstellar compound in which the N atom uses all five valence electrons [4]. The availability of synchrotron radiation and equivalent electron impact sources in recent times has served as an impetus for studies of photo-induced molecular processes, enabling measurements over wide spectral ranges and providing a wealth of data regarding the nature and properties of excited electronic states. Nitrous oxide is a case in point, understanding of its excited state structure and dynamics being greatly enhanced by studies carried out using a variety of experimental techniques [3–25] as well as theoretical calculations [26–35]. Nevertheless, a thorough understanding of the excited states of this molecule still remains a challenging problem.

The electronic absorption spectrum of N_2O spans a wide energy region, from the UV region ($45{,}000\ cm^{-1}$) and extending deep into the vacuum ultraviolet (VUV) region. In the VUV region, a number of electronic transitions comprising of both valence transitions and Rydberg series converging to the lowest two ionization limits at $\sim$12.89 and 12.91 eV (103,963 and 104,097 cm^{-1}) [17] are observed. The first VUV absorption spectrum of nitrous oxide was reported by Duncan in 1936 [6] and subsequently revisited by Sponer and Teller [7], Zelikoff et al. [8] and Tanaka et al. [9]. Early work on nitrous oxide is well summarized in the review by Rabalais et al. [10]. The only synchrotron radiation based photoabsorption study of this molecule was by Nee et al. [11] who reported absolute cross sections up to the first ionization potential, but no new spectral assignments were given. Additionally, there have also been a number of reports on the electronic spectrum of N_2O, focusing on specific aspects in small energy regions. For instance, photodissociation of N_2O through its first absorption band ($45{,}000$–$60{,}000\ cm^{-1}$) has received much attention in recent years due to its atmospheric implications [3,12–14,26–31]. In the 60,000–72,000 cm^{-1} region, after the initial work by Zelikoff et al. [8], there have been very few studies [15,16]. Vibronic assignments of the extensive and well formed progression of bands in this region are still incompletely understood. Towards the higher energy side of this progression ($>75{,}000\ cm^{-1}$), the absorption spectrum is dominated by Rydberg transitions. The Rydberg states of nitrous oxide have been studied by several authors using a variety of techniques like photoabsorption spectroscopy [9,11,15,17,18], resonance enhanced multiphoton ionization (REMPI) [19–22] and electron impact/electron energy loss spectroscopy [23–25]. Assignments of Rydberg series and accompanying vibronic structures reported in these papers are at wide variance with each other and a clear set of assignments is still not available. For example, the strong sharp band at $\sim$84,900 cm^{-1} has been assigned to the origin of the $3p\sigma\,^1\Pi$ transition in some works [17,24], and to the 3^1_0 vibronic band of $3p\sigma\,^1\Pi$ by others [19,20]. Although some of these discrepancies were resolved in the work by Cossart-Magos et al. [17], still several issues in assignments of transitions in the $85{,}000$–$95{,}000\ cm^{-1}$ region remain unresolved. From a theoretical perspective, the electronic spectroscopy of nitrous oxide presents many challenges with additional complications introduced due to perturbations like Renner–Teller coupling and spin–orbit splitting. There have been a wide range of theoretical studies covering various aspects like geometry and stability of its three isomers [26], photodissociation dynamics [27–31], excited electronic states [32–35], etc. A special mention must be made about the work by Hopper [34] which remains one of the most comprehensive theoretical studies of the electronic structure of nitrous oxide till date. Also worth citing are the frozen core calculations by Cossart-Magos et al. [17] which have helped in assigning many Rydberg transitions.

Despite this large volume of experimental and theoretical work, there remain several unresolved issues in the excited state electronic structure of nitrous oxide. The present work attempts to improve the understanding of the excited state structure of N_2O by carrying out a detailed reinvestigation of its VUV absorption spectrum. The photoabsorption spectrum of N_2O is recorded in the wavelength region $45{,}000$–$95{,}000\ cm^{-1}$ using synchrotron radiation. Ab initio calculations are used to aid the spectral analysis. Details of the experiment, computations and results obtained are discussed in the ensuing sections.

2. Methodology

2.1. Experimental

VUV photoabsorption studies were carried out using the Photophysics beamline coupled to the 450 MeV storage ring Indus-1 at Raja Ramanna Centre for Advanced Technology, Indore, India. Details of the experimental setup have been described in earlier papers [36,37]. Briefly, synchrotron radiation is dispersed by a 1 m Seya-Namioka monochromator with 2400 l/mm grating (resolving power $\sim$1000) and made to pass through a 25 cm long stainless steel gas cell. The experimental resolution is $\sim$6 meV ($\sim 48\ cm^{-1}$) at 6 eV and $\sim$12 meV ($\sim 97\ cm^{-1}$) at 12 eV. The cell is fitted with lithium fluoride windows, which limit the transmission to >1050 Å. Nitrous oxide of stated purity 99.9% procured from M/s. Alchemie Gases is used without further purification and introduced into the cell through a system of Swagelok valves. The transmitted intensity is detected using a sodium salicylate coated window and UV–visible photomultiplier tube. The measured intensity without sample serves as the reference or I_0 and the intensity with sample introduced serves as I. Using the Beer–Lambert law, a plot of $\ln(I_0/I)$ versus wavelength, scanned in steps of 0.5 Å generates the absorption spectrum. Spectra are recorded at several pressures in the range 0.001–10 mbar, measured using capacitance gauges. Due to the widely varying absorption cross sections in different wavelength regions, optimum pressures used also differ from region to region. The optimum pressures for obtaining clear absorption features in the sub-regions $50{,}000$–$62{,}000\ cm^{-1}$, $62{,}000$–$72{,}000\ cm^{-1}$ and $72{,}000$–$95{,}000\ cm^{-1}$ are found to be $\sim$10 mbar, 0.1 mbar and 0.001 mbar respectively. We however do not observe any noticeable change in the spectra when the pressure is varied in the neighborhood of these optimum pressures. The synchrotron beam current is recorded simultaneously at every step in order to normalize the data with respect to the decay in beam

current. Standard atomic lines of Xenon are used for calibration of the spectra.

2.2. Computational

N_2O is a 16 valence electron system with a linear $C_{\infty v}$ geometry, the ground state molecular orbital configuration being given by $1\sigma^2\ 2\sigma^2\ 3\sigma^2\ 4\sigma^2\ 5\sigma^2\ 6\sigma^2\ 1\pi^4\ 7\sigma^2\ 2\pi^4$: $^1\Sigma^+$. There have been several theoretical studies [26–35] on the electronic states of N_2O, the most exhaustive one being the work by Hopper in 1984 [34] reporting extensive MCSCF/CI calculations of several vertically excited singlet and triplet states as well as some potential energy surfaces. To the best of our knowledge there is no reported calculation of excited states up to the first ionization limit using the time dependent density functional theory (TD-DFT). Theoretical chemistry studies show that for excited state calculations, the TD-DFT method provides a good balance between numerical precision and computational cost [38]. In the present study we use the DFT and MP2 methods for geometry optimization and computation of vibrational wavenumbers of the neutral and ionic ground states, while TD-DFT calculations are used for prediction of vertical excited states. Basis sets used in the calculations include Pople's split valence basis set 6-31G(3d) with three d-type polarization functions [39], correlation consistent polarized basis sets of Dunning cc-pVnZ [40,41] and the polarization consistent basis sets of Jensen, pc-4 [42,43]. These families of basis sets are suitable for recovering the correlation energy, whereas the pc-4 basis is known to be particularly suited to density functional (DFT) calculations [43]. DFT computations are carried out using two hybrid exchange correlation GGA functionals viz. Perdew–Burke–Ernzerhof (PBE0) [44] and Becke-3–Lee–Yang–Parr (B3LYP) [45,46]. In particular, the PBE0 functional is known to perform well for excited state calculations [38] All calculations are done using the GAMESS (USA) suite of programs using parallel mode of computation when necessary [47]. Molecular orbital contour plots generated using the software MacMolPlt [48] for the highest occupied molecular orbitals (HOMO) and lowest unoccupied molecular orbitals (LUMO) of N_2O have been given as Supplementary material. The HOMO (2π) has an N–N bonding and N–O antibonding character while the LUMO (3π) is antibonding with respect to both N–N and N–O.

3. Results and discussion

3.1. Computational results

3.1.1. Geometry optimization and computation of vibrational frequencies

Geometry optimization of the ground state of N_2O is carried out using DFT as well as MP2 methods with several basis sets. The theoretically predicted vibrational frequencies using the DFT functional PBE0 and various basis sets are listed in Table 1 without any scaling factors. Difference between the calculated and observed [49] frequencies may be attributed to neglect of anharmonicity in the calculation. The geometry optimization of the ground state of N_2O^+ is also tabulated in Table 1. Calculated ionic frequencies often aid in the analysis of vibronic structure of Rydberg transitions as vibrational frequencies in excited Rydberg states are expected to be closer to vibrational frequencies of the corresponding ionic ground state rather than the ground state of the neutral molecule [50,51]. This approach which has been used successfully in some of our earlier works [36,37] to assign vibronic spectra is also employed in the present study. It is observed experimentally that in the ground state of the N_2O^+ ion, the molecule remains linear with an increase in R_{NN} bond length by 0.027 Å while the R_{NO} bond length remains almost the same as in the neutral molecule. This is also borne out by the N–N bonding and N–O antibonding character of the HOMO, from which the electron is removed.

3.1.2. Vertical excited state energies

Vertical excited states are calculated at the ground state optimized geometry using the TDDFT method. Calculations are performed for several basis sets and DFT functionals. The best results in terms of overall agreement with current experimental data and earlier theoretical work [34] are obtained for the PBE0 functional using the pc-4 basis set. Predicted singlet and triplet excited states up to ~14 eV (96,800 cm^{-1}) along with calculated oscillator strengths (O.S.) and lambda diagnostic values λ ($0 \le \lambda \le 1$) are presented in Table 2. The lambda diagnostic is a measure of

Table 1
Ground state geometry optimization and vibrational frequencies using DFT/PBE0.

Basis set	Energy (a.u.)	R_{NN} (Å)	R_{NO} (Å)	ν_1 (cm^{-1})	ν_2 (cm^{-1})	ν_3 (cm^{-1})
	Optimized parameters (N_2O: $X^1\Sigma^+$)					
6-311G(d)+	−184.5202	1.122	1.176	1376	593	2409
cc-pV5Z	−184.5555	1.117	1.175	1376	637	2404
pc-4	−184.5566	1.117	1.174	1376	637	2405
Experimental values[a]		1.127	1.185	1284.9	588.8	2223.8
Basis set	Optimized parameters (N_2O^+: $^2\Pi$)					
6-311G(d)+	−184.0583	1.135	1.178	1247	456	1890
cc-pV5Z	−184.0840	1.132	1.178	1246	498	1876
pc-4	−184.0850	1.132	1.177	1247	499	1876
Experimental values[b]		1.154	1.185	1127	457	1738

[a] [49].
[b] [53].

Table 2
Singlet and triplet vertical excited states of N_2O using TDDFT; PBE0/pc-4.

State	Predicted energy		Major transitions	O.S.	λ	Assignment/nature	Observed energy (eV)
	(cm^{-1})	(eV)					
$^3\Sigma^+$	42,296	5.244	$2\pi\rightarrow3\pi$	0.000	0.762	$a^3\Sigma^+$ (V)	–
$^3\Delta$	47,571	5.898	$2\pi\rightarrow3\pi$	0.000	0.481/0.768*	$b^3\Delta$ (V)	–
$^3\Sigma^-$	55,305	6.857	$2\pi\rightarrow3\pi$	0.000	0.487	$c^3\Sigma^-$ (V)	–
$^1\Sigma^-$	55,305	6.857	$2\pi\rightarrow3\pi$	0.000	0.487	$A^1\Sigma^-$ (V)	5.6–7.7
$^1\Delta$	58,411	7.242	$2\pi\rightarrow3\pi$	0.000	0.488/0.779*	$B^1\Delta$ (V)	
$^3\Pi$	67,557	8.376	$2\pi\rightarrow8\sigma$	0.000	0.390	$3s\sigma\,^3\Pi$ (R)	7.7–8.9
$^1\Pi$	70,630	8.757	$2\pi\rightarrow8\sigma$	0.000	0.389	$3s\sigma\ C^1\Pi$ (R)	
$^3\Pi$	76,405	9.473	$7\sigma\rightarrow3\pi$	0.000	0.616	$7\sigma\rightarrow\pi^*$(V)	
$^1\Sigma^+$	80,930	10.034	$2\pi\rightarrow3\pi$ $2\pi\rightarrow4$	0.423	0.539	$3p\pi\ D^1\Sigma^+$(R+V)	9.1–10.1
$^3\Sigma^+$	83,745	10.383	$2\pi\rightarrow4\pi$	0.000	0.391	(R)	–
$^3\Pi$	84,559	10.484	$2\pi\rightarrow9\sigma$	0.000	0.206	$3p\sigma\ ^3\Pi$ (R)	10.47
$^3\Delta$	84,898	10.526	$2\pi\rightarrow4\pi$	0.000	0.245/0.390*	(R)	–
$^1\Pi$	85,301	10.576	$2\pi\rightarrow9\sigma$	0.078	0.205	$3p\sigma\ ^1\Pi$ (R)	10.53
$^1\Delta$	85,963	10.658	$2\pi\rightarrow4\pi$	0.000	0.241/0.384*	(R)	–
$^1\Sigma^-$	86,245	10.693	$2\pi\rightarrow4\pi$	0.000	0.243	(R)	–
$^3\Sigma^-$	86,245	10.693	$2\pi\rightarrow4\pi$	0.000	0.243	$3p\pi\ ^3\Sigma^-$(R)	10.48
$^3\Sigma^+$	89,116	11.049	$1\pi\rightarrow3\pi$	0.000	0.788	(V)	–
$^1\Pi$	92,568	11.477	$7\sigma\rightarrow3\pi$; $2\pi\rightarrow10\sigma$	0.022	0.522	$7\sigma\rightarrow\pi^*$(V+R)	10.84
$^3\Pi$	93,173	11.552	$2\pi\rightarrow10\sigma$	0.000	0.234	$4s\sigma\ ^3\Pi$ (R)	10.94
$^1\Pi$	94,036	11.659	$2\pi\rightarrow10\sigma$; $7\sigma\rightarrow3\pi$	0.050	0.320	$4s\sigma\ ^1\Pi$ (R)	11.05
$^3\Delta$	94,730	11.745	$1\pi\rightarrow3\pi$	0.000	0.471/0.751*	(V+R)	–
$^3\Sigma^+$	97,617	12.103	$2\pi\rightarrow5\pi$	0.000	0.328	(R)	–
$^3\Pi$	98,553	12.219	$2\pi\rightarrow10\sigma$; $2\pi\rightarrow11\sigma$	0.000	0.423	$4p\sigma\ ^3\Pi$ (R)	11.74
$^1\Sigma^+$	98,763	12.245	$7\sigma\rightarrow8\sigma$; $2\pi\rightarrow4\pi$	0.267	0.426	$4p\pi\ ^1\Sigma^+$ (R)	11.64
$^3\Delta$	98,964	12.270	$2\pi\rightarrow5\pi$	0.000	0.237/0.378*	(R)	–
$^1\Delta$	99,045	12.280	$2\pi\rightarrow5\pi$	0.000	0.179/0.287*	(R)	–
$^3\Sigma^-$	99,400	12.324	$2\pi\rightarrow5\pi$	0.000	0.185	$4p\pi\ ^3\Sigma^-$ (R)	11.74
$^1\Sigma^-$	99,400	12.324	$2\pi\rightarrow5\pi$	0.000	0.188	(R)	–
$^3\Sigma^+$	100,303	12.436	$7\sigma\rightarrow8\sigma$	0.000	0.268	(R)	–
$^1\Sigma^+$	101,505	12.584	$2\pi\rightarrow5\pi$	0.104	0.303	(R)	–
$^1\Sigma^+$	102,634	12.725	$7\sigma\rightarrow8\sigma$	0.312	0.291	(R)	–
$^3\Sigma^-$	103,981	12.892	$1\pi\rightarrow3\pi$	0.000	0.519	(V)	–
$^1\Sigma^-$	103,981	12.892	$1\pi\rightarrow3\pi$	0.000	0.519	(V)	–
$^1\Pi$	104,578	12.962	$1\pi\rightarrow12\sigma$; $2\pi\rightarrow12\sigma$	0.001	0.423	(R)	–
$^1\Delta$	107,247	13.297	$1\pi\rightarrow3\pi$	0.000	0.527/0.841*	(V)	–
$^3\Pi$	109,982	13.636	$7\sigma\rightarrow3\pi$	0.000	0.578	(V)	–
$^3\Sigma^+$	111,603	13.837	$7\sigma\rightarrow9\sigma$	0.000	0.268	(R)	–
$^1\Pi$	112,434	13.940	$2\pi\rightarrow11\sigma$; $2\pi\rightarrow12\sigma$	0.046	0.403	$4p\sigma\ ^1\Pi$ (R)	11.76

λ: Lambda diagnostic, (R): Rydberg, (V): valence; and O.S.: oscillator strength.
* Two values of λ are for the two components of the degenerate Δ states.

the spatial overlap in a given excitation [52]. A relatively large value of λ implies short range excitations, or a large overlap between the occupied and virtual orbitals, whereas a relatively small value of λ implies long range excitations. In the present study the lambda diagnostic value is used as an estimate of the valence or Rydberg character of the transition. In general, large values of λ (>0.6) imply valence character, small values (<0.3) imply Rydberg character and intermediate values (0.3–0.6) may be due to a mixed character (cf. Table 2). However, these values are used in conjunction with the nature of the final orbital involved in the transition. In the present work, we find that although most Rydberg transitions are predicted with lambda value of <0.3, there are a few transitions which are clearly Rydberg type from the nature of the final orbital, but predicted with $\lambda=0.3$–0.4. In the case of N_2O it is found that when the final orbital is 3π, the transition is typically valence in nature, whereas for 4π 8σ, 9σ, 10σ … the excited state is Rydberg in nature (cf. Table 2). Valence–Rydberg mixed transitions are those for which there are two excitations predicted with comparable amplitude, typically one of valence type and the other of Rydberg type.

3.1.3. *Potential energy curves for excited singlet states*

Some insight into the geometries and dynamics of the excited states can be gained by studying their potential

energy curves (PECs). PECs for excited singlet states are obtained with respect to change in bond angle, change in N–N bond length and change in N–O bond length, while keeping other geometrical parameters fixed to the ground state equilibrium values. Fig. 1 (a, b and c) shows the potential energy curves up to the first few singlet excited states plotted with respect to N–N bond length r_1, N–O bond length r_2 and N–N–O bond angle θ respectively. It may be noted that the present study is reported in terms of θ, whereas some of the earlier studies [27,30,32] used the Jacobi angle γ. The two angles are related by a simple relation of the form: $\theta=\gamma+\sin^{-1}(r_1 \sin\gamma/2r_2)$. To the best of our knowledge, this is the first report of PECs of N_2O generated using the TDDFT method although PECs of N_2O have been reported using other methods [30–32]. The PECs for the first few excited states agree well with earlier reports [30–32], while extending the work to higher excited states.

3.2. Experimental observations and correlation with computational results

The experimentally observed VUV absorption spectrum of N_2O recorded using the Photophysics beamline at Indus-1 is shown in Fig. 2 and may be distinguished into four major regions. Analysis and interpretation of the absorption bands are discussed in the following sections, aided by theoretical calculations wherever relevant. The correspondence of theoretically predicted excitation energies and experimentally observed bands is based on initial and final state molecular orbitals involved as well as comparison of the O–C values. We may mention here that the accuracy of the calculated values is expected to be very good in the energy region up to HOMO+1 eV [38], which in the present case corresponds to ~10.85 eV. Above this energy, the agreement with experimental values becomes somewhat poorer.

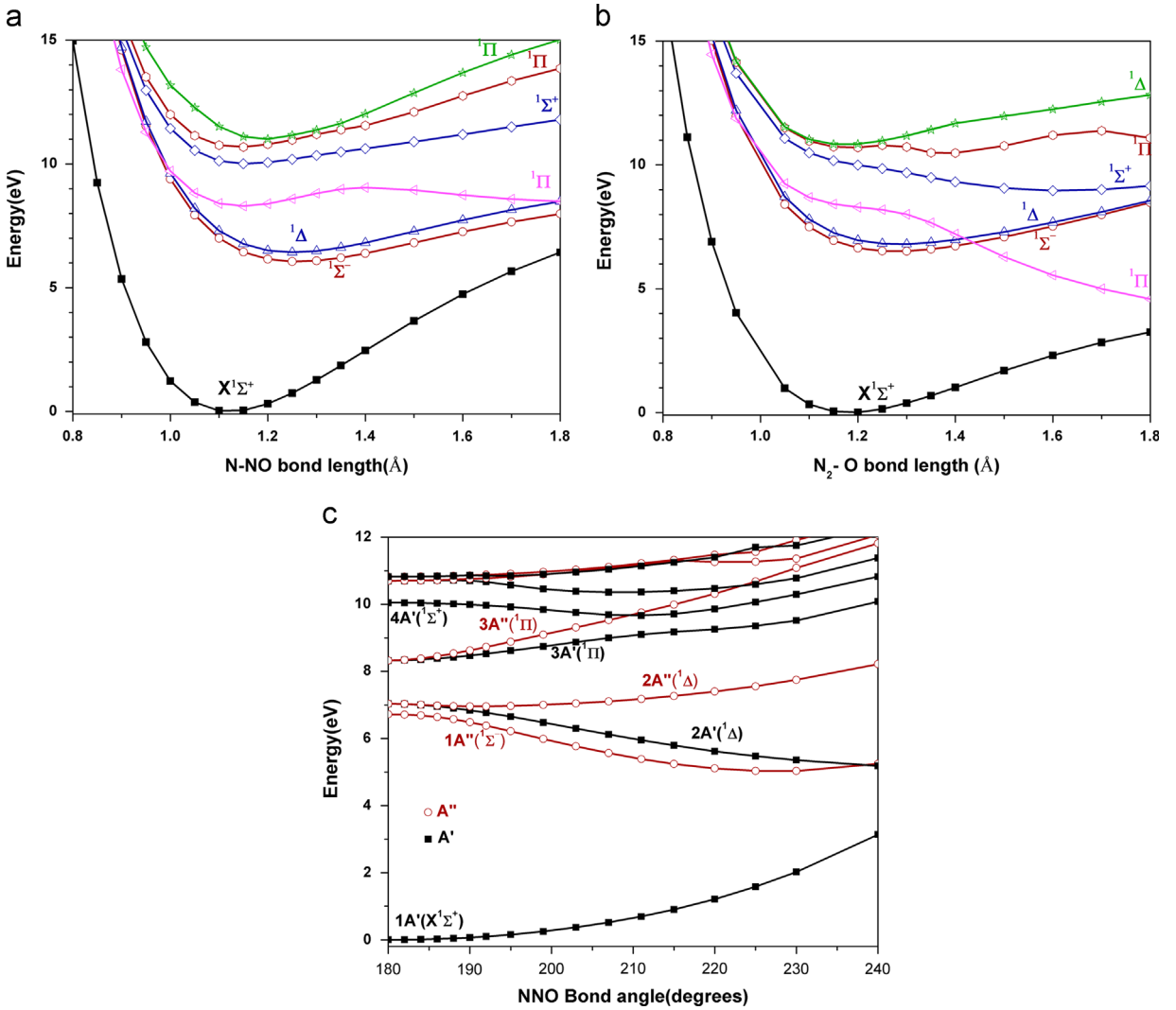

Fig. 1. Potential energy curves of the first few excited states of N_2O. (a, b and c) Plotted with respect to N–NO bond length, N_2–O bond length and NNO bond angle respectively.

3.2.1. The energy region 5.6–7.7 eV (45,000–60,000 cm^{-1})

At relatively low pressures (<1 mbar), the absorption system observed in this region appears as a continuum, but as the pressure is increased (>1 mbar), vibronic bands appear, superimposed on the continuum (cf. Fig. 3). There have been several recent experimental and theoretical studies of this region covering various aspects such as temperature and isotopic substitution effects, product angular distributions, potential energy surfaces, etc. [14,27–29,31]. In an earlier work by us, a partial listing of prominently observed bands had been reported [15]. The first two singlet excited states of N_2O are $A^1\Sigma^-$ and $B^1\Delta$ (cf. Table 2), transitions to both of which are forbidden under $C_{\infty v}$ symmetry. In the Franck-Condon region, the molecule is non-linear in the excited state and exhibits C_s symmetry. The observed absorption spectrum is ascribed to transitions from the linear ground state X $^1\Sigma^+$ to the $^1A''$ ($^1\Sigma^-$) state and the $^1A'$ and $^1A''$ Renner–Teller components of the $^1\Delta$ state, both of which are allowed under C_s symmetry [3,14,27]. The underlying continuum is due to the dissociative natures of the $^1\Sigma^-$ state and A′ component of the $^1\Delta$ state, as evident from the potential energy curve with respect to bond angle (cf. Fig. 1c).

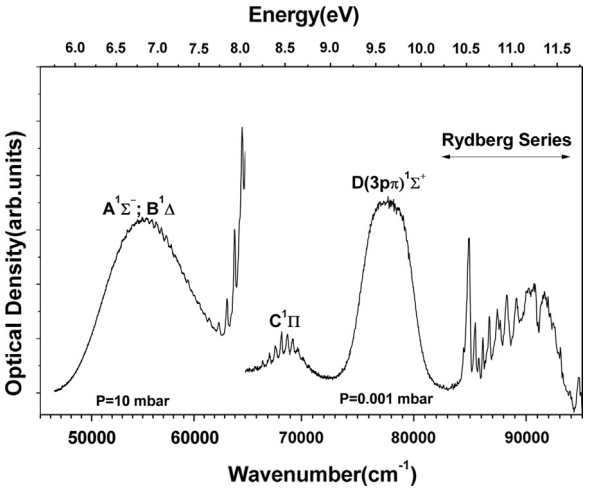

Fig. 2. The VUV photoabsorption spectrum of N_2O in the 45,000–95,000 cm^{-1} region.

It has been established [27] that the vibronic structures in this region arise predominantly from A′ ($^1\Delta$) state, with a smaller contribution from the A″ ($^1\Delta$) state. In this context, it is instructive to examine the variation of oscillator strength with the N–N–O bond angle as plotted in Fig. 4a. One sees that there is an appreciable gain in oscillator strength for the A′ (Δ) state, whereas there is a very small increase in oscillator strength for the A″ (Σ^-) and A″ (Δ) states (cf. inset in Fig. 4a). This could be the reason why the continuum arising from the repulsive A′ (Δ) state is much stronger than the overriding vibrational structure. The observed vibronic features correspond to excitation of the ν_2 bending mode in the excited electronic state, although the diffuseness of the bands has been attributed to large amplitude NN bond stretching [27]. It has also been discussed earlier [3,14,27] that the observed structure is dominated by hot band transitions from the (0,1,0) and (0,2,0) levels with the ratios of oscillator strengths for vibronic transitions going as $\sigma(\nu_2''=1)/\sigma(\nu_2''=0) = 2$ and $\sigma(\nu_2''=2)/\sigma(\nu_2''=1) = 2.9$ [27]. In the present work, two major series are identified (cf. Table 3). On the basis of the observed separation of $\sim$588 cm^{-1} (ground state value of ν_2) between the two progressions and earlier theoretical simulations [27], we infer that these are hot band progressions from (0,1,0) and (0,2,0) (cf. Fig. 3), rather than the fundamental. A few weaker and diffuse features on the higher energy side could be members of the fundamental progression from (0,0,0). The extreme diffuseness of the bands in this region prevents a clear assignment of the series; hence these bands are excluded from Table 3. A measured average separation of $\sim$478 cm^{-1} between successive members of

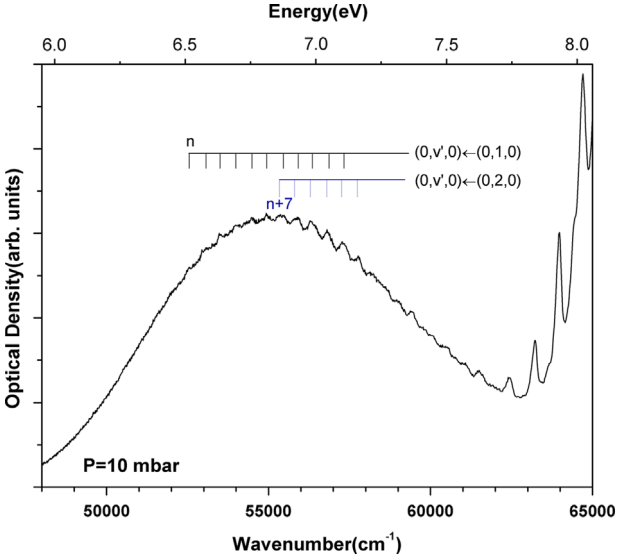

Fig. 3. Part of the VUV absorption spectrum of N_2O showing vibronic assignments in the 45,000–65,000 cm^{-1} region. *n* Refers to the quanta of bending vibration in the excited state υ_2'.

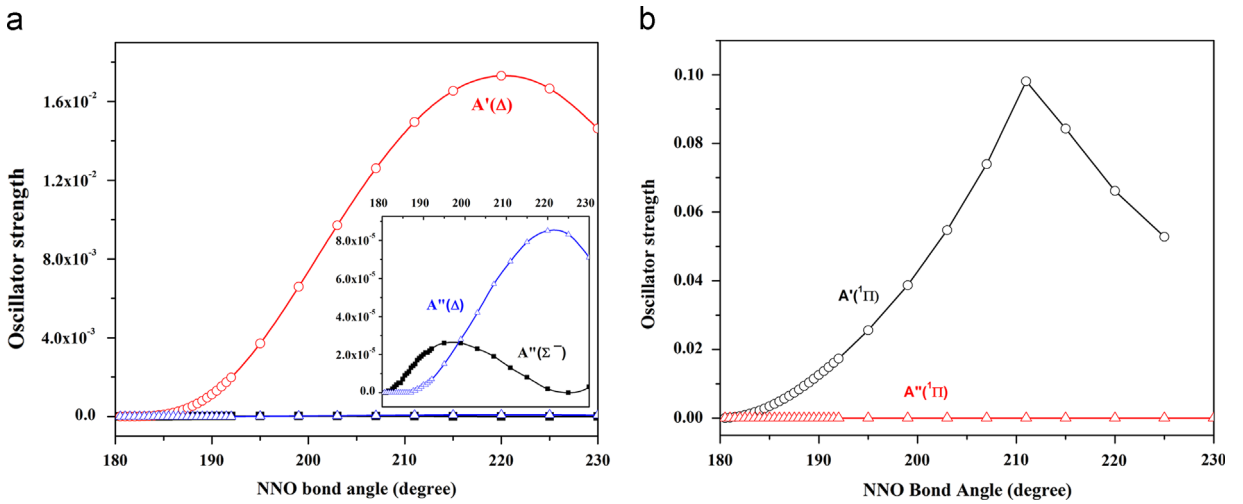

Fig. 4. Variation of oscillator strength with bending angle for low lying excited states of N_2O.

Table 3
Vibronic bands observed (cm^{-1}) in the photoabsorption spectrum of N_2O in the 52,000–60,000 cm^{-1} region.

v'	($v''=1$)	($v''=2$)
n	52,545	
$n+1$	53,060	
$n+2$	53,504	
$n+3$	53,978	
$n+4$	54,477	
$n+5$	54,939	
$n+6$	55,453	
$n+7$	55,909	55,322
$n+8$	56,340	55,810
$n+9$	56,850	56,288
$n+10$	57,330	56,797
$n+11$	57,779	57,264
$n+12$	–	57,752
$n+13$	–	58,184
ω	479	477

a progression is consistent with the interpretation of these structures arising predominantly from excitation of the ν_2' mode.

3.2.2. The energy region 7.7–8.85 eV (~60,000–72,000 cm^{-1})

The electronic transition observed in this region is accompanied by a well formed progression of bands and corresponds to the classically designated transition $X^1\Sigma^+$–$C^1\Pi$. This transition is correlated with the theoretically predicted excited state at 8.759 eV (70,646 cm^{-1}) which arises from the orbital excitation $2\pi\rightarrow 8\sigma$ (cf. Table 2). In concurrence with the interpretation by Hopper [34], this excited state may be assigned to the first member of the ns Rydberg series $3s\sigma^1\Pi$ converging to the (adiabatic) IP 104,097 cm^{-1} ($^2\Pi_{1/2}$), with a quantum defect of ~1.37.

Tentative assignments of the observed vibronic bands have been proposed in earlier literature [6–8,16]. The earliest work by Duncan [6] reported a few bands of average spacing 621 cm^{-1}, proposing that the value of 621 cm^{-1} may either represent a reduction of the stretching frequency ν_1 or an increase in bending frequency ν_2 in the excited state. As early as 1941, the possibility of two progressions arising from a degenerate upper state split due to interaction between electronic and vibrational motions was also suggested by Sponer and Teller [7]. Later, Zelikoff et al. [8] reported 21 bands which they fitted to single progression assuming a fundamental stretching frequency of 1005 cm^{-1} and an unusually high value of anharmonicity in the upper state. A recent paper by Zhen et al. [16] reports a jet-cooled study of six bands, restricted to the region above 67,000 cm^{-1} assigning the observed bands to the ν_2' bending mode. The bands observed in the present work are listed in Table 4 and shown in Fig. 5. The separation between successive bands is observed to be irregular and decreases rather rapidly, from a value of about 1000 cm^{-1} to ~500 cm^{-1} (cf. Table 4). This unusual structure cannot be satisfactorily explained in terms of any of the known vibrational frequencies of nitrous oxide either as a single ν_2 progression, for which the initial value of 1000 cm^{-1} seems too high, or as a single ν_1 progression, for which one has to assume a very high anharmonicity. While the possibility of multiple progressions cannot be completely ruled out, we propose that most of the observed bands can be fitted to a ν_2 progression, provided one assumes a Renner–Teller interaction in the excited $^1\Pi$ (degenerate) electronic state. Although the predicted oscillator strength for a vertical transition to the $C^1\Pi$ state at equilibrium geometry is zero (cf. Table 2), as the molecule executes a bending vibration the $^1\Pi$ state splits into $^1A'$ and $^1A''$ states, of which the A' component is seen to gain considerable oscillator strength as the molecule deviates from linearity (cf. Fig. 4b). Therefore, it is very likely that the electronic transition is accompanied primarily by excitation of the bending mode (which is also responsible for its observed intensity), with a possibility of smaller contribution from stretching modes. The Renner–Teller interaction couples the vibrational angular momentum l of the bending mode with the electronic orbital angular momentum Λ [51] as described below.

Table 4
Assignment of vibronic bands observed (cm^{-1}) in the $X^1\Sigma^+$–$C^1\Pi$ system of N_2O including the Renner–Teller interaction in the excited state.

v_2'	$l=0$, $K=1$			$l=2$, $K=1$		
	Calculated	Observed	O–C	Calculated	Observed	O–C
0	60,308	60,450	142			
2	61,057	61,078	21	61,374	61,462	88
4	61,822	61,612	−210	62,371	62,429[a]	58
6	62,566	62,429[a]	−137	63,342	63,232[a]	−110
8	63,287	63,232[a]	−55	64,290	64,430	140
10	63,986	63,972	−14	65,214	65,227	13
12	64,662	64,707	45	66,114	66,087	−27
14	65,314	65,406	92	66,991	67,007	16
16	65,943	65,913	−30	67,845	67,698[a]	−147
18	66,549	66,565	16	68,676	68,746	70
20	67,132	67,163	31	69,483	69,535	52
22	67,692	67,698[a]	6	70,268	70,195	−73
24	68,229	68,236	7	71,029	70,990[a]	−39
26	68,742	68,746	4	Molecular parameters of $C^1\Pi$ state		
28	69,233	69,228	−5	Parameter	Value	Error
30	69,700	69,701	1	0_0^0	59,851 cm^{-1}	±25
32	70,144	70,106	−38	ω_2	467 cm^{-1}	±1.5
34	70,564	70,540	−24	x_{22}	−2.9	±0.08
36	70,962	70,990[a]	28	ε	−0.24	±0.008

[a] Blended lines, O–C – difference in observed and calculated energy.

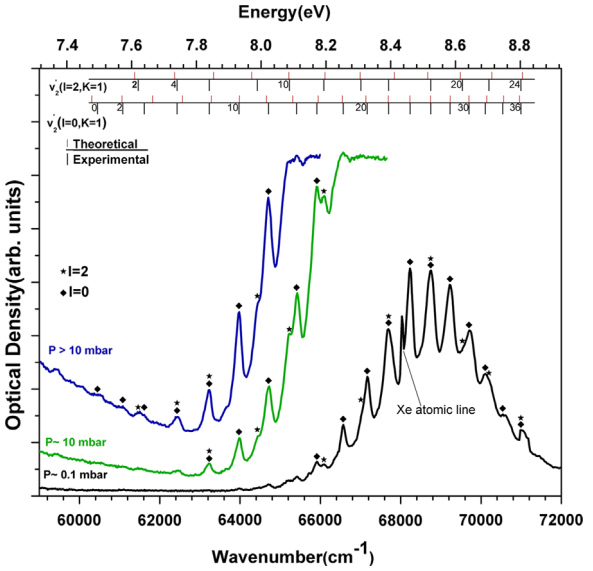

Fig. 5. VUV absorption spectrum of N_2O showing Renner–Teller coupled vibronic band assignments in the 60,000–72,000 cm^{-1} region.

The general expression for vibronic term values of a linear triatomic molecule is given by

$$G(v_1,v_2,v_3)=\sum_i \omega_i\left(v_i+\frac{d_i}{2}\right)+\sum_i\sum_{k>i}x_{ik}\left(v_i+\frac{d_i}{2}\right)\left(v_k+\frac{d_k}{2}\right)+\sum_i\sum_{k>i}g_{ik}l_il_k \quad (1)$$

where $G(v_1,v_2,v_3)$ is the vibronic energy in cm^{-1}, ω_i are the vibrational frequencies, x_{ik} and g_{ik} are the anharmonicity constants, l_i is the vibrational angular momentum and d_i is the degeneracy of the ith mode. For the bending vibration ω_2, the vibrational energy level expression (1) reduces to

$$G(v_2,l)=\{\omega_2(v_2+1)+g_{22}l^2\}+x_{22}(v_2+1)^2 = G^{\pm}(v_2,K)+x_{22}(v_2+1)^2 \quad (2)$$

Due to the Renner–Teller interaction, the resultant angular momentum is given by $K=l+\Lambda$ and the interaction terms $G^{\pm}(v_2,K)$ may be written as

$$K=0;\quad G^{\pm}(v_2,0)=\omega_2\sqrt{1\pm\varepsilon}(v_2+1),\quad v_2=1,3,5\ldots \quad (3)$$

$$K\neq 0,\quad v_2=K-1;\quad G(v_2,K)=\omega_2\left[(v_2+1)-\frac{1}{8}\varepsilon^2K(K+1)\right] \quad (4)$$

$$K\neq 0,\quad v_2>K-1;\quad G^{\pm}(v_2,K)=\omega_2(1-\frac{1}{8}\varepsilon^2)(v_2+1)\pm\frac{1}{2}\omega_2\varepsilon\sqrt{(v_2+1)^2-K^2} \quad (5)$$

where ε is the Renner–Teller interaction parameter. Selection rules for the vibronic transitions are given in terms of the standard group theoretical notation for dipole allowed transitions [51]; viz. $\Gamma(\psi_{e'v'})\otimes\Gamma(\psi_{e''v''})\supseteq\Gamma(M)$. Further, for the case of vibronic coupling, we consider only the dipole moment components characterizing the allowed electronic transition $\Sigma^+\rightarrow\Pi$ [51]. Thus, only those vibronic transitions are allowed for which the direct product of the symmetry species of the initial and final vibronic wavefunctions transforms as (x,y). Since the initial electronic state is of Σ^+ symmetry, only vibronic levels of Π symmetry are allowed. Further, since levels of Π symmetry arise only from the Renner–Teller interaction between Π electronic state and vibrational levels of even quantum number v_2', the selection rules effectively allow only transitions with even vibrational quantum number v_2'

Table 5
Transitions observed in the VUV photoabsorption spectrum of N_2O in the 75,000–95,000 cm^{-1} region.

Peak[a]	Assignment	Q.D	Peak[b]	Assignment	Peak[c]	Assignment	Peak[d]	Assignment	Peak[e]	Assignment	Peak[f]	Assignment
77,600	$3p\pi^1\Sigma^+$	0.96	–	$3p\pi^1\Sigma^+$	77,520	$D^1\Sigma^+$						
							82,725	$3p\sigma^3\Pi$	83,026		82,743	$3_1^1\ 3p\sigma^1\Pi$
											83,042	$2_1^1\ 3p\sigma^1\Pi$
					83,264	$3p\sigma^1\Pi$	83,178	$3p\sigma^1\Pi$	83,188	$0_0^0\ 3p\pi^1\Delta$	83,200	$0_0^0\ 3p\sigma^1\Pi$
									83,356	$2_1^1\ \Delta(N2O^+?)$		
83,433	$2_2^0\ 3p\sigma^3\Pi$											
									83,621	$2_1^2\ \Sigma^+$	83,628	$2_0^1\ 3p\sigma^1\Pi$
83,915	$2_1^0\ 3p\sigma^3\Pi$								83,911	$2_0^1\ \Delta$		
									84,057	$2_0^2\ \Phi$	84,061	$2_0^2\ 3p\sigma^1\Pi$
									84,330	$1_0^1\ 3p\sigma^1\Pi$	84,339	$1_0^1\ 3p\sigma^1\Pi$
84,439	$0_0^0\ 3p\sigma^3\Pi$	0.63	84,379	$3p\sigma^3\Pi$								
			84,631	$3p\pi^3\Sigma^-$					84,780	$3_0^1 2_1^1$		
84,910	$0_0^0\ 3p\sigma^1\Pi$	0.61	84,918	$0_0^0\ 3p\sigma^1\Pi$	84,818	$3_0^1\ 3p\sigma^1\Pi$			84,937	$3_0^1\ 3p\sigma^1\Pi$	84,927	$3_0^1\ 3p\sigma^1\Pi$
85,464	$2_0^1\ 3p\sigma^1\Pi$		85,482	$2_0^1\ 3p\sigma^1\Pi$	85,397	$1_0^1\ 3p\sigma^1\Pi$			85,441		85,465	$1_0^2\ 3p\sigma^1\Pi$
85,788	$3p\pi^3\Sigma^-$	0.55										
86,152	$3_0^1\ 3p\sigma^3\Pi$		86,122	$3_0^1\ 3p\sigma^3\Pi$							86,012	$0_0^0\ 3p\pi^1\Sigma^+;^1\Delta$
86,362(w)												
86,512(sh)									86,478			
86,714	$3_0^1\ 3p\sigma^1\Pi$		86,670	$3_0^1\ 3p\sigma^1\Pi$	86,655	$3_0^2\ 3p\sigma^1\Pi$			86,643		86,700	$1_0^3\ 3p\sigma^1\Pi$
86,979(w)											86,900	$3_0^2\ 3p\sigma^1\Pi$
87,198(sh)											87,122	$1_0^1\ 3p\pi^1\Sigma^+;^1\Delta$
87,433	$7\sigma\rightarrow3\pi^1\Pi$				87,336	$1_0^2\ 3p\sigma^1\Pi$					87,438	$0_0^0\ 3d\sigma^1\Pi$
87,685	$2_1^0\ 4s\sigma^3\Pi$										87,712	$3_0^1\ 3p\pi^1\Sigma^+;^1\Delta$
88,004(sh)											88,027	$0_0^0\ 3d\pi^1\Sigma^+;^1\Delta$
88,265	$4s\sigma^3\Pi$	1.36	88,262	$4s\sigma^3\Pi$	88,183	$3_0^3\ 3p\sigma^1\Pi$						
88,436(sh)	$2_1^0\ 4s\sigma^1\Pi$											
88,778(w)												
89,130	$4s\sigma^1\Pi$	1.29	89,150	$4s\sigma^1\Pi$								
89,243(w)												
					88,968	$3d\delta^1\Pi^1\Phi$					88,972	$0_0^0\ 3d\delta^1\Pi^1\Phi$
89,512(w)												
89,750	$2_0^1\ 4s\sigma^1\Pi$											
90,036	$3_0^1\ 4s\sigma^3\Pi$											
90,230	$1_0^1\ 4s\sigma^1\Pi$											
90,510												
90,737	$3_0^1\ 4s\sigma^1\Pi$				90,662							
91,050	$1_0^1 3_0^1\ 4s\sigma^3\Pi$											
91,382	$1_0^2\ 4s\sigma^1\Pi$						91,283	$4s\sigma^3\Pi$				
91,493	$2_0^1 3_0^1\ 4s\sigma^1\Pi$						91,443	$4s\sigma^1\Pi$				
91,623	$3_0^2\ 4s\sigma^3\Pi$				91,575							
91,784	$3d\ \delta^3\Pi$	−0.002										
91,952	$3d\ \delta^1\Pi$	−0.006										
92,142	$3d\sigma^3\Pi$	−0.05										
92,395	$3d\sigma^1\Pi$	−0.06										
	$3d\pi^1\Sigma^+$	−0.08										
92,563(sh)	$3d\pi^3\Sigma^-$	−0.08										
92,861	$2_0^1\ 3d\pi^3\Sigma^-$											
93,030	$2_0^1\ 3d\pi^1\Sigma^+$											
93,236	$1_0^1\ 3d\sigma^3\Pi$											
93,880	$4p\pi^1\Sigma^+$	0.70					93,904	$4p\sigma^3\Pi$				
94,040 (w)			94,085	$4p\pi^1\Sigma^+$	94,158	$4p\sigma^1\Pi$	94,075	$4p\sigma^1\Pi$				
								$4p\pi^3\Sigma^+$				
94,696	$4p\sigma^3\Pi$	0.56	94,696	$4p\sigma^3\Pi$								
	$4p\pi^3\Sigma^-$	0.58										
			94,755	$4p\pi^3\Sigma^-$			94,705	$4p\pi^3\Sigma^+$				
94,872	$4p\sigma^1\Pi$	0.55	94,896	$2_1^1\ 4p\sigma^1\Pi$			94,903	$4p\pi^1\Sigma^+$				
			94,910	$4p\sigma^1\Pi$								

Q.D.: quantum defect; $^1\Sigma^+$ and $^3\Pi$ converge to $^2\Pi_{3/2}$ at 103,963 cm^{-1}; $^3\Sigma^-$ and $^1\Pi$ converge to $^2\Pi_{1/2}$ at 104,097 cm^{-1}.

[a] Present study.
[b] [17].
[c] [11].
[d] [21].
[e] [20].
[f] [19].

and may be arranged into two groups ($l=0$, $K=1$) and ($l=2$, $K=1$). Initial values for the Renner–Teller parameter ε and anharmonicity constant x_{22} in the excited state are assumed to be close to those of the ground state of the N_2O^+ ion [53]. Using the above Eqs. (2)–(5), most of the observed bands in the $C^1\Pi$ system can be fitted to within $\pm 150\ cm^{-1}$ as listed in Table 4 and marked in Fig. 5.

From a fitting of the experimental data, molecular parameters for the $C^1\Pi$ state are obtained as $\omega_2=467\ cm^{-1}$, $x_{22}=-2.9$ and $\varepsilon=-0.24$. The more intense and prominent peaks are due to the $l=0$ progression whereas the $l=2$ members appear as shoulders. The deviations between observed and calculated values are within reasonable limits considering the inherent diffuse nature of the bands and blending of $l=0$ and $l=2$ members at certain positions. It is generally seen that there are larger deviations for the weaker and more diffuse band whereas the sharper and intense bands fit well. The diffuseness of the bands has also been observed in the jet cooled study by Zhen et al. [16] and explained as due to a superposition of bending and fast dissociative stretching mode of $C^1\Pi$ state along the N–O coordinate. The repulsive behavior of the potential curve with respect to N–O stretch (cf. Fig. 1b) reinforces this argument. In this context, it is also observed that a few of the bands in this region, viz. 59,430, 60,450, 61,612, 62,429 cm^{-1} follow a ν_1' progression with average separation of $\sim 1000\ cm^{-1}$. Thus the picture of a prominent ν_2' progression showing Renner–Teller splitting, along with some contribution from ν_1', explains the vibronic structure satisfactorily. Considering the inherent diffuse nature of the bands with band widths of the order $\sim 200\ cm^{-1}$, the fitting accuracy of $\pm 150\ cm^{-1}$ is quite satisfactory.

3.2.3. The energy region 8.9–10.2 eV ($\sim$72,000–82,000 cm^{-1})

A single highly intense and broad peak is observed in this region ($\sim$77,600 cm^{-1}). This peak which has been observed in earlier photoabsorption studies [11] was assigned to the $3p\pi\,^1\Sigma^+$ Rydberg transition converging to the (adiabatic) IP 103,963 cm^{-1} ($^2\Pi_{3/2}$) by Cossart-Magos et al. [17]. The rather high quantum defect value of 0.96 (cf. Table 5) obtained for this transition is uncharacteristic of a p-type Rydberg state and had been attributed to a bond bending stabilization effect by Cossart-Magos et al. [17]. If we consider the theoretically predicted excitation energies and oscillator strengths (cf. Table 2), the only excited state in this energy region with high oscillator strength is the $D^1\Sigma^+$ state at 10.034 eV (80,930 cm^{-1}). Dominant contributions to this transition are from 2π–3π (valence) to 2π–4π (Rydberg), with lambda diagnostic value of 0.539. Thus, we may be justified in concluding that the $D^1\Sigma^+$ has a mixed valence–Rydberg character, thereby explaining the unusual quantum defect. At all pressures used, no vibronic features are distinguished riding on the continuum. From the potential energy plots (cf. Fig. 1a–c) it can be seen that in the vertical excitation region, the $D^1\Sigma^+$ state shows a repulsive behavior with respect to bond angle, while exhibiting shallow minima with respect to bond lengths. This saddle point behavior is probably the cause for the broad diffuse nature of this band with lack of vibrational structure.

3.2.4. The energy region 10.2–11.8 eV ($\sim$82,000–95,000 cm^{-1})

The energy region 82,000–95,000 cm^{-1} (cf. Fig. 6) is dominated by richly structured Rydberg series converging to the spin–orbit components of the ionic ground state of N_2O at 103,963 cm^{-1} ($^2\Pi_{3/2}$) and 104,097 cm^{-1} ($^2\Pi_{1/2}$) [17]. Previous studies of this region include several REMPI experiments [19–21], photoabsorption studies with lab sources [9,17] and with synchrotron radiation source [11]. In this energy region 75,000–104,000 cm^{-1}, the work by Cossart-Magos et al. [17] is the most extensive study available, in which several Rydberg series are assigned based on frozen core calculations. In the present work, several distinct bands are observed with good intensity which are either absent or reported as weak in their work. Rydberg series and vibronic structures observed in the present study are listed in Table 5 along with previous studies for comparison. Quantum defects (Q.D.) calculated in the present study are also indicated in Table 5. As can be seen from Table 5, there is considerable discrepancy in spectral assignments made by different authors [11,17,19–21]. In the present study, we attempt to sort out some of the discrepancies and arrive at a consistent set of assignments as discussed in what follows.

Rydberg series observed in N_2O are due to transitions from the ground state to excited orbitals of type $nl\lambda$. Since the excitation is primarily from the HOMO 2π orbital, it can be seen that the $ns\sigma$, $np\sigma$ and $nd\sigma$ series give rise to $^{1,3}\Pi$ states, whereas the $np\pi$ and $nd\pi$ series give rise to $^{1,3}\Sigma^\pm$ and $^{1,3}\Delta$ states. Similarly, the $nd\delta$ series give rise to $^{1,3}\Pi$ and $^{1,3}\Phi$ states. From electric dipole selection rules, only transitions to $^1\Sigma^+$ and $^1\Pi$ states are expected to appear in the photoabsorption spectrum. However due to spin–orbit coupling, triplet states also become allowed. The $^3\Pi_{2,1}$ series converge to the spin–orbit split ionic state $^2\Pi_{3/2}$

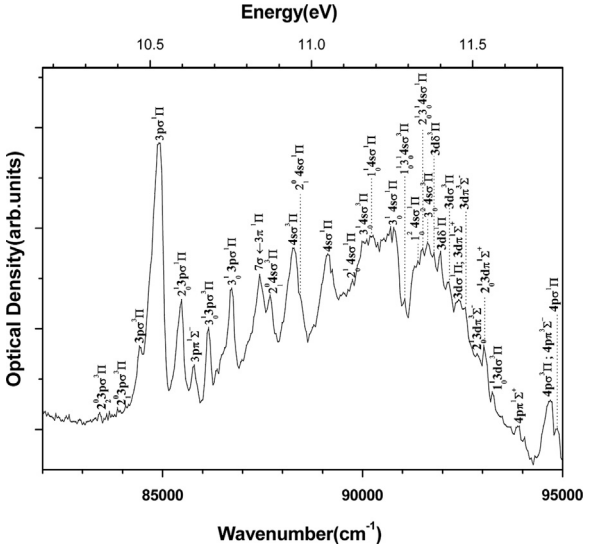

Fig. 6. VUV absorption spectrum of N_2O showing Rydberg series in the 82,000–95,000 cm^{-1} region.

whereas $^3\Pi_0$ and $^1\Pi_1$ converge to the ionic state $^2\Pi_{1/2}$. [54,17]. In the case of Σ states arising from a $\pi\rightarrow\pi^*$ excitation, the spin orbit operator couples states with opposite behavior with respect to the σ_v operator, i.e. Σ^+ is coupled to Σ^- [54]. Thus, transitions from the $^1\Sigma^+$ ground state become allowed to excited states of $^1\Sigma^+$ and $^3\Sigma^-$ symmetry through the spin–orbit mixing mechanism and $^1\Sigma^+$ series converge to $^2\Pi_{3/2}$, whereas the $^3\Sigma^-$ series converge to $^2\Pi_{1/2}$ [53,17]. It is worth mentioning here that, for most of the Rydberg transitions observed, triplet states appear with intensity comparable to that of singlets. This is an indication of strong spin–orbit coupling (Hund's case c) which one would normally expect only for high n Rydberg states. In the present study which is restricted to the region below 95,000 cm^{-1} we have observed $n=3$ and 4 members of these series. Assignments have been largely made based on the calculated quantum defect values reported by Cossart-Magos et al. [17]. It may be noted that the adiabatic ionization energies 103,963 cm^{-1} and 104,097 cm^{-1} from pulsed field ionization studies [55] are used throughout in the Rydberg series analysis.

3.2.4.1. nsσ Series. The first member of this series, viz. 3sσ $^{1,3}\Pi$ lies in the 7.7–8.85 eV (62,000 to 70,000 cm^{-1}) region and has been discussed in Section 3.2.2. The next higher member of this series, viz. 4sσ $^{3,1}\Pi$, is observed at 88,265 and 89,130 cm^{-1} (cf. Fig. 6) with quantum defects of 1.36 and 1.29 respectively. These states arise from the $2\pi\rightarrow10\sigma$ orbital excitation and are theoretically predicted at 11.552 and 11.659 eV (93,173 and 94,036 cm^{-1}) (cf. Table 2). The peak at 87,685 cm^{-1} may be assigned to the hot band transition $2_1^0$4sσ$^3\Pi$ due to population of the ν_2 bending mode at room temperature. The corresponding hot band of the 4sσ $^1\Pi$ transition (88,436 cm^{-1}) appears as a shoulder to the intense 4sσ$^3\Pi$ peak.

3.2.4.2. npσ and npπ Series. The 3pσ configuration gives rise to the 3pσ $^{3,1}\Pi$ states which are observed at 84,439 and 84,910 cm^{-1} correspondingly with a quantum defect of ~0.6. The intensity of the triplet transition is considerably less than that of the corresponding singlet transition, thus indicating a weak spin–orbit coupling. These states can be identified with the theoretically predicted vertical excited states at 10.484 and 10.576 eV (84,559 and 85,301 cm^{-1}) corresponding to the orbital excitation $2\pi\rightarrow9\sigma$. The assignment of the origin of the 3pσ $^1\Pi$ transition in literature has been controversial. In some of the earlier REMPI works [19,20], the 84,910 cm^{-1} band has been assigned to 3_0^1 3pσ $^1\Pi$ with the origin of the Rydberg transition being located at 83,200 cm^{-1}, whereas other works [17,24] have assigned the 84,910 cm^{-1} peak to the origin of 3pσ $^1\Pi$. From the current photoabsorption study, we observe that the peak at 84,910 cm^{-1} is the most intense in the entire 83,000–95,000 cm^{-1} region, whereas no line is observed at 83,200 cm^{-1} at any of the pressures used, reaffirming the assignment of the origin to 84,910 cm^{-1}. The large value of predicted oscillator strength (cf. Table 2) for the 3pσ $^1\Pi$ transition supports the validity of this assignment. Two weak but distinct bands at 83,433 cm^{-1} and 83,915 cm^{-1} are observed to the lower wavenumber side of the strong 84,910 cm^{-1} band, at relatively higher pressures. These bands are assigned to the hot band transitions $2_1^0$3pσ$^3\Pi$ and $2_2^0$3pσ$^3\Pi$. Vibronic bands corresponding to excitation of the ν_2 and ν_3 modes in the excited 3pσ $^{3,1}\Pi$ states are observed at 85,464, 86,152 and 86,714 cm^{-1} as listed in Table 5. The next pair of this series, 4pσ $^{3,1}\Pi$, appear at 94,696 cm^{-1} and 94,872 cm^{-1} with a quantum defect of ~0.55. Theoretically, the triplet component is predicted at 12.219 eV (98,553 cm^{-1}), while the singlet component is predicted at 13.94 eV (112,434 cm^{-1}), based on the orbital excitations involved. This discrepancy in experimental and theoretical values may be due the spin–orbit coupling which is not accounted for in the theoretical model used.

The 3pπ$^1\Sigma^+$ state has been assigned to the strong and broad band observed at ~77,600 cm^{-1} as discussed in Section 3.2.3. The corresponding 3pπ $^3\Sigma^-$ state is assigned to a weak feature at 84,631 cm^{-1} by Cossart-Magos et al. [17]. In the present study no peak is observed at 84,631 cm^{-1}. The 3pπ $^3\Sigma^-$ state is theoretically predicted at 10.693 eV (86,245 cm^{-1}), to the higher energy side of the 3pσ $^1\Pi$ state by about 940 cm^{-1} (cf. Table 2). We therefore assign the peak observed at 85,788 cm^{-1} (cf. Fig. 6) to 3pπ $^3\Sigma^-$. It may be noted that this peak was not observed in the work by Cossart-Magos et al. [17], while other more intense spectral features in this region are reported as weak features by them. The obtained quantum defect of 0.55 confirms the assignment of this peak to a p state. The next pair of this series, viz. 4pπ$^1\Sigma^+$ and 4pπ$^3\Sigma^-$, are observed at 93,880 and 94,696 cm^{-1} with quantum defects of 0.70 and 0.58 respectively. Correspondence of 4pπ$^3\Sigma^-$ to the theoretically predicted transition at 12.324 eV (99,400 cm^{-1}) is straightforward. On the other hand, it is seen that 4pπ$^1\Sigma^+$ can be correlated with the theoretically predicted energies at 12.245 eV (98,763 cm^{-1}) or 12.584 eV (101,505 cm^{-1}) based on orbital excitations. (cf. Table 2). As one goes to higher Rydberg states, complications due to multiple orbital excitations and spin–orbit interaction render unambiguous correspondence of experimental and theoretical values difficult.

3.2.4.3. ndσ, ndπ and ndδ Series. There is considerable discrepancy in assignment of the 3d states in earlier works. Although Cossart-Magos et al. have predicted the 3dλ transitions to lie in the region ~90,000–92,500 cm^{-1}, they have not been able to experimentally identify any clear peaks [17]. In the earlier REMPI-PES study by Scheper et al. [21] observed peaks at 91,283 and 91,443 cm^{-1} have been assigned to 4sσ $^{3,1}\Pi$. However, the theoretical calculations of Cossart-Magos et al. [17] suggest that this region corresponds to excitation to the 3d Rydberg series. Moreover, as explained by them, the PES experiments may not correctly predict the symmetry of the excited Rydberg state. Patsilinakou et al. [19] have assigned 3dλ (λ=σ,π,δ) origins to peaks at 87,438, 88,027 and 88,972 cm^{-1}. This implies a quantum defect of ~0.29–0.42, which seems too high for a d state. In the present studies, several clear and distinct peaks are observed in this region as seen in Fig. 6. Based on the calculated quantum defect values and the observed positions of the higher members ($n=4$, 5) [17], we reassign the observed peaks in this region to singlet and triplet components of the 3dλ states. The five peaks

from 91,784 cm^{-1} to 92,563 cm^{-1} are assigned to 3dλ states as given in Table 5. The quantum defects obtained are in the range −0.002 to −0.08, which is in agreement with the theoretical values of Cossart-Magos et al. [17], thus confirming the validity of the present assignments. Most of the remaining bands in this region which could be assigned to vibronic features accompanying the Rydberg series 4sσ and 3dπ (cf. Table 5).

3.2.4.4. Valence excitations. The distinct feature observed at 87,433 cm^{-1} has been reported in a few earlier works [11,18,19]; however assignments made by these authors are not in agreement with each other. Assuming the frozen core calculations of Cossart-Magos et al. [17] to be the best theoretical estimate of quantum defects available, these features cannot be satisfactorily assigned to any Rydberg transition. We therefore propose that this peak is a valence transition $X^1\Sigma^+ \rightarrow {}^1\Pi$ arising from the orbital excitation $7\sigma \rightarrow 3\pi^*$. This transition is theoretically predicted at 11.477 eV (92,568 cm^{-1}) with a lambda diagnostic value of 0.522, confirming its valence nature. The triplet component arising from this orbital excitation is predicted at 9.473 eV (76,405 cm^{-1}), which overlaps with the strong, broad peak at ~77,700 cm^{-1}. It may be noted that our assignments are consistent with the prediction of valence transitions at 78,900 ($^3\Pi$) and 91,300 ($^1\Pi$) cm^{-1} by Cossart-Magos et al. [17] although they have not reported any experimental peaks corresponding to these transitions.

4. Conclusions

In this paper we have presented a photoabsorption study of nitrous oxide in the VUV region (45,000–95,000 cm^{-1}) using synchrotron radiation. Quantum chemical calculations of excited state energies, oscillator strengths and potential energy curves are performed in order to gain a better understanding of the excited state structure. The observed spectrum consists of a few valence transitions and several Rydberg series ($n=3, 4$) converging to the two spin–orbit components ($^2\Pi_{3/2,1/2}$) of the ground state of N_2O^+. The first absorption system (45,000–60,000 cm^{-1}) is ascribed to the forbidden states $^1\Sigma^-$ and $^1\Delta$, made allowed by change in geometry of the molecule to a bent configuration in the excited states. The underlying strong continuum observed is attributed to the large gain in oscillator strength of the transition to the repulsive A′ (Δ) state as the molecule bends. A pressure dependent study of this region enabled identifying and assigning several hot band transitions (originating from $\nu_2''=1, 2$) involving the $\nu_{2'}$ bending mode whose frequency is measured to be ~478 cm^{-1} in the excited state. The interpretation of the $C^1\Pi$ electronic state (60,000–72,000 cm^{-1}) as the 3s Rydberg transition is supported by theoretical predictions. The irregular spacing of vibronic features of the $X^1\Sigma^+ \rightarrow C^1\Pi$ absorption system is explained for the first time as arising due to a Renner–Teller interaction. Molecular parameters ($\omega_2=467$ cm^{-1}, $x_{22}=-2.9$, $\varepsilon=-0.24$) obtained by fitting the observed bands to the Renner–Teller expressions seem to be reasonable considering the value of ω_2 in the ionic state and other excited states of N_2O are close to 467 cm^{-1} and the Renner–Teller parameter in the ionic ground state is ~ −0.2.

To the higher energy region, the broad and intense 3pπ $^1\Sigma^+$ transition at ~77,600 cm^{-1} is proposed to have a mixed valence–Rydberg character, explaining its unusually high quantum defect value of 0.96. In the 84,000–95,000 cm^{-1} region dominated by Rydberg series, several features are observed and assigned for the first time. In this region, the comprehensive experimental data supported by extensive theoretical calculations have resulted in unambiguous assignments and clarification of discrepancies in earlier work. The 3pπ $^3\Sigma^-$ Rydberg state at 85,788 cm^{-1}, the valence transition $7\sigma \rightarrow 3\pi$ ($^1\Pi$) at 87,433 cm^{-1} and the 3dλ Rydberg series in the 91,700–92,600 cm^{-1} region as well as several accompanying vibronic transitions are assigned for the first time. The intensity of singlets and triplets being comparable for most of the observed Rydberg states leads to the conclusion that the spin–orbit coupling is quite large in Rydberg states of N_2O, even for low n (3,4). A few transitions in the 90,000–95,000 cm^{-1} region remain unassigned. A clearer picture may emerge by carrying out synchrotron radiation based photoabsorption studies at higher resolution and using better theoretical models. This paper provides a consolidated view and at the same time presents fresh insights into the VUV photoabsorption spectrum of nitrous oxide, which could form useful inputs for future work related to the excited state dynamics of this atmospherically important molecule.

Appendix A. Supporting information

Supporting data associated with this article can be found in the online version at http://dx.doi.org/10.1016/j.jqsrt.2014.05.017.

References

[1] Ravishankara AS, Daniel JS, Portmann RW. Nitrous oxide (N_2O): the dominant ozone depleting substance emitted in the 21st century. Science 2009;326:123–5.
[2] Wuebbles DJ. Nitrous oxide: no laughing matter. Science 2009;326:56–7.
[3] Kawamata H, Kohguchi H, Nishide T, Suzuki T. Photodissociation of nitrous oxide starting from excited bending levels. J Chem Phys 2006;125:133312-1–10.
[4] Bustos E, Velasco AM, Martin I, Lavin C. Photoabsorption of nitrous oxide through Rydberg states in the bound and continuum regions. J Phys Chem A 2002;106:35–40.
[5] Carlon NR, Papanastasiou DK, Fleming EL, Jackman CH, Newman PA, Burkholder JB. UV absorption cross sections of nitrous oxide (N_2O) and carbon tetrachloride (CCl_4) between 210 and 350 K and the atmospheric implications. Atmos Chem Phys 2010;10:6137–49.
[6] Duncan ABF. The far ultraviolet absorption spectrum of N_2O. J Chem Phys 1936;4:638–41.
[7] Sponer E, Teller E. Electronic spectra of polyatomic molecules. Rev Mod Phys 1941;13:76–170.
[8] Zelikoff M, Watanabe K, Inn ECY. Absorption coefficients of gases in the vacuum ultraviolet. Part II. Nitrous oxide. J Chem Phys 1953;21:1643–7.
[9] Tanaka Y, Jursa AS, Leblanc FJ. Higher ionization potentials of linear triatomic molecules. II. CS_2, COS and N_2O. J Chem Phys 1960;32:1205–14.
[10] Rabalais JW, McDonald JM, Scherr V, McGlynn SP. Electronic spectroscopy of isoelectronic molecules. II. Linear triatomic

groupings containing sixteen valence electrons. Chem Rev 1971;71:73–108.
[11] Nee JB, Yang JC, Lee PC, Wang XY, Kuo CT. Photoabsorption cross sections of N_2O in 100–220 nm. Chin J Phys 1999;37:172.
[12] von Hessberg P, Kaiser J, Engoff MB, McLinden CA, Sorensen SL, Röckmann T, et al. Ultraviolet absorption cross sections of isotopically substituted nitrous oxide species: $^{14}N^{14}NO$, $^{14}N^{15}NO$, $^{15}N^{14}NO$ and $^{15}N^{15}NO$. Atmos Chem Phys 2004;4:1237–53.
[13] Yoshino K, Freeman DE, Parkinson WH. High resolution absorption cross section measurements of N_2O at 295 to 299 K in the wavelength region 170–222 nm. Planet Space Sci 1984;32:1219–22.
[14] Selwyn GS, Johnston HS. Ultraviolet absorption spectrum of nitrous oxide as function of temperature and isotopic substitution. J Chem Phys 1981;74:3791–803.
[15] Shastri A, Sunanda K, Singh P, Raja Sekhar BN, Souza RD', Bhaskara Rao SVN, et al. Excited state vibrational modes of a few triatomic molecules of environmental interest [special issue]. Asian J Spectrosc 2012:121–41.
[16] Zhen C, Hu Y, Zhou X, Liu S. Dissociation dynamics of nitrous oxide from jet-cooling absorption spectrum in 142.5–147 nm. Chin J Chem Phys 2011;24:267–74.
[17] Cossart-Magos C, Jungen M, Launay F. High resolution absorption spectrum of N_2O between 75,000 and 104,000 cm^{-1}. J Chem Phys 2001;114:7368–78.
[18] Lee LC, Suto M. Production and quenching of excited photofragments of N_2O. J Chem Phys 1984;80:4718–26.
[19] Patsilinakou E, Wiedmann RT, Fotakis C, Grant ER. Jet resolved vibronic structure in the higher excited states of N_2O: ultraviolet three photon absorption spectroscopy from 80,000 to 90,000 cm^{-1}. J Chem Phys 1989;91:3916–25.
[20] Szarka MG, Wallace SC. Spectroscopy and photodissociation of Rydberg states of N_2O. J Chem Phys 1991;95:2336–51.
[21] Scheper CR, Kuijit J, Buma WJ, de Lange CA. Resonance-enhanced multiphoton ionization photoelectron spectroscopy of Rydberg states of N_2O below the $X\,^2\Pi$ ionization limit. J Chem Phys 1998;109:7844–50.
[22] Maul C, Poretskiy M, Rakhymzhan A, Grunenberg J. On the ultraviolet absorption spectrum of nitrous oxide and its van der Waals complexes. J Mol Spectrosc 2009;256:80–5.
[23] Wang YY, Sun JM, Zhu LF. Cross sections for the valence shell excitations of nitrous oxide studied by fast electron impact. J Chem Phys 2010;132:124301.
[24] England K, Reddish T, Comer. Electron energy loss studies of nitrous oxide in the energy range 10–20 eV. J. Chem Phys 1988;119:435–41.
[25] Ya-Wei L, You-Yan W, Lin-Fan Z. Valence shell excitations of nitrous oxide studied by fast electron impact. Chin Phys Lett 2012;29:043302-1–3.
[26] Wang F, Harcourt R. Electronic structure study of the N_2O isomers using post-Hartree–Fock and density functional theory calculations. J Phys Chem A 2000;104:1304–10.
[27] Schinke R. Photodissociation of N_2O: potential energy surfaces and absorption spectrum. J Chem Phys 2011;134:064313.
[28] McBane GC, Schinke R. Product angular distributions in the ultraviolet photodissociation of N_2O. J Chem Phys 2012;136:044314.
[29] Schinke R, Schmidt JA. Photodissociation of N_2O: excitation of $^1A''$ states. J Phys Chem A 2012;116:11083–7.
[30] Brown A, Jimeno P, Balint-Kurti GG. Photodissociation of N_2O. I. Ab initio potential energy surfaces for the low-lying electronic states $X\,^1A'$, $2\,^1A'$and $1\,^1A''$. J Phys Chem A 1999;103:11089–95.
[31] Nanbu S, Johnson MS. Analysis of the ultraviolet absorption cross section of six isotopically substituted nitrous oxide species using 3D wavepacket propagation. J Phys Chem A 2004;108:8905–13.
[32] Daud MH, Balint-Kurti GG, Brown A. Ab initio potential energy surfaces, total absorption cross sections, and product quantum state distributions for the low-lying electronic states of N_2O. J Chem Phys 2005;122 (054305-1-9).
[33] Winter NW. Theoretical assignments of the electronic states of nitrous oxide. Chem Phys Lett 1975;33:300–4.
[34] Hopper DG. Ab *initio* multiple root optimization MCSCF study of the $C_{\infty v}/C_s$ excitation spectra and potential energy surfaces of N_20. J Chem Phys 1984;80:4290–316.
[35] Martín I, Velasco M, Lavín C, Olalla E, Bustos E. Photoabsorption processes in nitrous oxide and formaldehyde. Int J Quant Chem 2001;85:345–53.
[36] Shastri A, Singh P, Raja Sekhar BN, Souza RD', Jagatap BN. The role of torsional modes in the electronic absorption spectrum of acetone. J Quant Spectrosc Radiat Transf 2012;113:1553–65.
[37] Singh P, Shastri A, Raja Sekhar BN, Souza RD', Jagatap BN. Effect of isotopic substitution in the electronic absorption spectrum of acetone: VUV photoabsorption studies of acetone-d_6. J Quant Spectrosc Radiat Transf 2013;114:20–8.
[38] Ciofini I, Adamo C. Accurate evaluation of valence and low-lying Rydberg states with standard time-dependent density functional theory. J Phys Chem A 2007;111:5549–56.
[39] Francl MM, Pietro WJ, Hehre WJ, Binkley JS, Gordon MS, DeFrees DJ, et al. Self-consistent molecular orbital methods XXIII. A polarization-type basis set for second-row elements. J Chem Phys 1982;77:3654–65.
[40] Dunning TH. Gaussian basis set for use in correlated molecular calculations. I. The atoms boron through neon and hydrogen. J Chem Phys 1989;90:1007–23.
[41] Woon DE, Dunning Jr TH. Gaussian basis set for use in correlated molecular calculations. III. The atoms aluminum through argon. J Chem Phys 1993;98:1358–71.
[42] Jensen F. Polarization consistent basis sets. II. Estimating the Kohn–Sham basis set limit. J Chem Phys 2002;116:7372–9.
[43] Jensen F. Polarization consistent basis sets. V. The elements Si–Cl. J Chem Phys 2004;121:3463–70.
[44] Perdew JP, Burke K, Ernzerhof M. Generalized gradient approximation made simple. Phys Rev Lett 1996;77:3865–8.
[45] Lee C, Yang W, Parr RG. Development of the Colle–Salvetti correlation energy formula into a functional of the electron density. Phys Rev B 1988;37:785–9.
[46] Becke AD. Density-functional thermochemistry. III. The role of exact exchange. J Chem Phys 1993;98:5648–52.
[47] Schmidt MW, Baldridge KK, Boatz JA, Elbert ST, Gordon MS, Jensen JH, et al. General atomic and molecular electronic structure system. J Comput Chem 1993;14:1347–63.
[48] Bode BM, Gordon MS. MacMolPlt: a graphical user interface for GAMESS. J Mol Gr Model 1998;16:133–8.
[49] Herzberg G. Molecular spectra and molecular structure, vol. II. Princeton, New Jersey: Infrared and Raman Spectra, D Van Nostrand Company Inc.; 1966.
[50] Robin MB. Higher excited states of polyatomic molecules, vol. I. New York: Academic Press; 1974.
[51] Herzberg G. Molecular spectra and molecular spectra vol III electronic spectra and electronic structure of polyatomic molecules. Princeton, New Jersey: D Van Nostrand Company; 1966.
[52] Peach MJG, Benfield P, Helgaker T, Tozer DJ. Excitation energies in density functional theory: an evaluation and a diagnostic test. J Chem Phys 2008;128:044118-1–8.
[53] Callomon JH, Creutzberg F. The electronic emission spectrum of ionized nitrous oxide N_2O^+: $A^2\Sigma^+$–$X^2\Pi$. Philpos Trans R Soc 1971;277:157–89.
[54] Lefebvre-Brion H, Field RW. The spectra and dynamics of diatomic molecules. Amsterdam: Elsevier; 2004.
[55] Wiedmann RT, Grant ER, Tonkyn RG, White MG. High resolution photoionization of N_2O. J Chem Phys 1991;95:746–53.